

Polymorphic Phase Control Mechanism of Organic–Inorganic Hybrid Perovskite Engineered by Dual-Site Alloying

Jiwon Jeon,[†] Taedaeheong Eom,[†] Eunyeong Lee,[‡] Sol Kim,[‡] Sanghak Kim,[‡] Ki-Ha Hong,^{*,§} and Hyungjun Kim^{*,†}

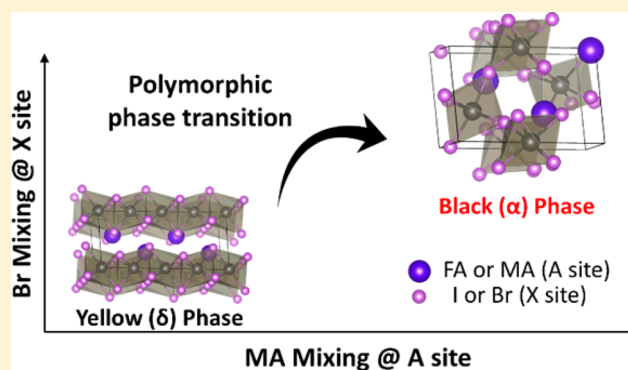
[†]Graduate School of EEWS, Korea Advanced Institute of Science and Technology (KAIST), 291 Daehak-Ro, Yuseong-Gu, Daejeon 34141, Korea

[‡]Central Advanced Research & Engineering Institute, Hyundai Motor Company, 37 Cheoldobangmulgwan-ro, Uiwang-si, Gyeonggi-do 16082, Korea

[§]Department of Materials Science and Engineering, Hanbat National University, 125 Dongseo-Daero, Yuseong-Gu, Daejeon 34158, Korea

Supporting Information

ABSTRACT: As a next-generation solar cell, perovskite solar cells (PSCs) have been attracting considerable attention. FAPbI₃ is particularly considered as an optimal material with a proper band gap and thus has been employed as a base material for the PSCs with more than 20% efficiency; however, the competitive polymorphic growth of α - and δ -phases is a major hurdle in utilizing this material. To provide the theoretical model of the polymorphic phase competition of FAPbI₃ for the first time, we here investigate how compositional engineering can pave a route to control the polymorphic growth of FAPbI₃ using density functional theory combined with a statistical-mechanical treatment of the configurational space. We find that dual-site alloying of both cations and halides is critically important to achieve the specific stabilization of the α -phase while maintaining the good miscibility, thermodynamic stability, and optimal band gap property. Based on our first successful theoretical modeling of the FAPbI₃ system and its polymorphic phase competition behavior during dual-site alloying, we anticipate deriving new rational guidelines on compositional engineering of organic–inorganic hybrid perovskite alloys for designing PSCs with high efficiencies and stabilities.



1. INTRODUCTION

As low-carbon energy is imperative for sustainable and clean power production in the future, considerable attention has been paid to light harvesting technologies capable of direct conversion of solar energy into electricity. In particular, there have been intensive developments in perovskite solar cells (PSCs) in recent years, accompanied by a substantial improvement of the power conversion efficiency (PCE). In the seminal work reported in 2009, the methylammonium lead triiodide perovskite (MAPbI₃) was used as a light sensitizer of the dye-sensitized solar cells (DSSCs), resulting in a PCE of 3.81%.¹ In 2012, it was revealed that a perovskite material can directly serve as an active material for solar cells instead of as a light sensitizer, showing a dramatically enhanced PCE of 9.7%.² Since then, many researchers have elucidated the working mechanism^{3,4} and developed fabrication methods^{5,6} and device structures^{7,8} to optimize the material's properties. These efforts have led to a rapid improvement of the photovoltaic performance of PSCs, with the PCE increasing from 9.7% to 22.1%.^{2,9–15}

In addition to the remarkable improvement in the PCE, other features of the PSCs—potentially low-cost raw material, inexpensive processing, and design versatility—add advantages when employing PSCs in fields such as building construction and vehicle manufacture. In order to realize this, PSCs with a high durability and stability are essential, and it is important to improve the thermal stability of multicomponent organic–inorganic hybrid perovskite materials.

Actually, perovskite is a general term defining the structure family with a mineral composition of ABX₃; the A-site is for a cation coordinated by 12 X anions, and the B-site is for a metal bonded to 6 X anions, forming corner-sharing BX₆ octahedra in a three-dimensional framework. Thus, the composition engineering of perovskite materials has been a major strategy in developing high-performance PSCs by varying the building blocks of the A-, B-, and X-sites. For example, substituting Br for

Received: April 4, 2017

Revised: April 11, 2017

Published: April 12, 2017

the I of MAPbI₃ widens the band gap from 1.55 to 2.3 eV,^{1,2,16} allowing for band gap tailoring using a halide mixed perovskite: MAPb(I_{1- χ _{Br}}Br _{χ _{Br}})₃ ($0 < \chi_{\text{Br}} < 1$).^{17–19} Additionally, Noh et al.¹⁷ demonstrated that the stability of MAPbI₃ can be significantly improved by the mixing of Br into halide sites. Previous theoretical studies showed that bromide perovskites could offer better trap densities and phase stabilities over iodide perovskites.^{6,20}

More interestingly, it has been considered that further optimized material properties can be achieved by replacing the methylammonium cation (MA) with the larger formamidinium cation (FA) at the A-site. Compared to MAPbI₃, with a band gap of 1.55 eV,^{1,2,21} FAPbI₃ has a smaller band gap of 1.48 eV (~840 nm absorption),²¹ yielding a higher photon conversion efficiency. Eperon et al. demonstrated that FAPbI₃ is stable even at 150 °C in air,²¹ implying a more enhanced thermal stability than MAPbI₃. Furthermore, the undesirable *J*–*V* hysteresis (observed in MAPbI₃-based PSCs²²) was efficiently suppressed in FAPbI₃-based PSCs.²³

Despite such ideal material properties, the major obstacle to the successful use of FAPbI₃ in PSCs arises from the polymorphic growth of FAPbI₃.²² At room temperature, FAPbI₃ has two polymorphs: a black trigonal (*P3m1*) phase (namely, α -phase) and a yellow hexagonal (*P6₃mc*) phase (namely, δ -phase).^{22,24} Unlike the trigonal phase consisting of a three-dimensional network of corner-sharing PbI₆ octahedrons (i.e., perovskite structure; Figure 1a), the hexagonal phase is a layered structure consisting of linear chains of face-sharing octahedrons (i.e.,

nonperovskite structure; Figure 1b). Since the hexagonal phase has a wider band gap, which is detrimental to solar cell efficiency, it becomes critical to suppress the hexagonal phase formation.

Either a cation alloying at the A-site (FA with MA or Cs)^{25–27} or a simultaneous cation and halide alloying at both A- and X-sites^{11,14,28–31} is considered to be effective in stabilizing the trigonal phase of FAPbI₃ over the hexagonal phase, thereby enhancing the performance of PSCs. When both MA and Br are cosubstituted into FAPbI₃, it has been reported that the hexagonal phase disappeared completely, as confirmed from X-ray diffraction (XRD) measurements.¹¹ Also, a markedly enhanced stability up to 250 h has been reported for PSCs using ternary alloying of FA/MA/Cs at the A-site and I/Br alloying at the X-site.³⁰

Although the simultaneous mixing at A- and X-sites has been the key strategy to fabricate PSCs with high efficiencies of over 20%,³⁰ its mechanistic origin is still not clearly understood and has not been theoretically explored yet. Previous theoretical studies were mostly about the MAPbI₃ system, where no polymorphic growth issue exists, and thereby no modeling efforts on the FAPbI₃ system and its polymorphic phase competition behavior during dual-site alloying have been pursued, to our best knowledge. Also, despite it being the simpler case of Br mixing only at the X-site of FAPbI₃ compared to dual-site alloying, there is no theoretical attempt to explain the experimental discovery of the thin film quality of FAPb(I_{1- χ _{Br}}Br _{χ _{Br}})₃ depending on the Br content; the good crystallinity of FA-based-PSCs with mixed halides can be obtained only at the I- and Br-rich condition,³² which can be modulated by further mixing elements at the A-site.²⁹

To realize a rational design and property tailoring of mixed perovskite systems, in this study, we pursue a comprehensive theoretical investigation into how alloying at the A- and X-sites can control the polymorphic phase behavior between trigonal and hexagonal phases of FAPbI₃, which is directly related to the efficiencies and thermal stabilities of FA-based-PSCs. We identify the individual and cooperative roles of A-site mixing and X-site mixing on the phase stabilization and polymorphism of α -FAPbI₃, and we discuss principles that can be useful in designing compositions of mixed perovskites with enhanced efficiency and stability.

2. COMPUTATIONAL DETAILS

2.1. Density functional theory calculations. We use first-principles-based density functional theory (DFT) calculations, which have been widely utilized in the field, to reveal the fundamental and unique properties of solar cell materials.^{33–41} We first calculated formation energies and cell parameters of various existing and nonexisting polymorphic phases of FAPbI₃ and MAPbI₃, namely, cubic, tetragonal, trigonal, and hexagonal, as summarized in Table 1. We used the generalized gradient approximation (GGA) of the PBEsol functional⁴² implemented in the Vienna Ab initio Simulation Package (VASP) with the choice of plane wave cutoff energy of 400 eV. The convergence criteria of the self-consistent field iteration and ionic relaxation were set as 10⁻⁶ eV and 10⁻² eV/Å, respectively.

2.2. Configurational ensemble average. When multiple elements competitively occupy the lattice sites after alloying, the configurational space dramatically expands, and thus, an ensemble average over the configurational space becomes unavoidable for the accurate calculation of enthalpy and entropy. Thus, the thermodynamic arguments based on the ensemble

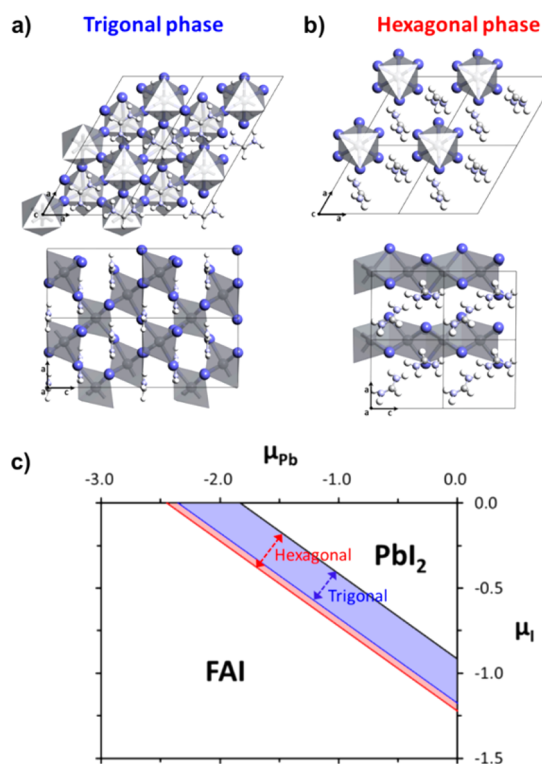


Figure 1. DFT optimized structures and phase diagram showing polymorphic growth of FAPbI₃. (a) Black trigonal phase (perovskite phase) and (b) yellow hexagonal phase (nonperovskite phase) of FAPbI₃ obtained from DFT calculations. (c) Thermodynamic stable range for equilibrium growth of FAPbI₃. Chemical potential ranges where the trigonal phase is stable (blue) and the hexagonal phase is stable (red) overlap, indicating the polymorphic growth of both phases.

Table 1. DFT Results of FAPbI₃ and MAPbI₃: DFT Optimized Cell Parameters, Equilibrium Volume per ABX₃ Unit (V), and Formation Enthalpy per ABX₃ Unit (ΔH_f) for Various Phases of FAPbI₃ and MAPbI₃^a

	cell parameters						V (Å ³ /f.u.)	ΔH_f (eV/f.u.)
	a (Å)	b (Å)	c (Å)	α (deg)	β (deg)	γ (deg)		
FAPbI₃								
Tetragonal	8.578	9.007	12.751	89.87	89.96	89.32	246.26	-4.644
Trigonal	8.986 (8.9817)	9.004 (8.9817)	10.702 (11.0062)	89.99 (90)	90.01 (90)	120.12 (120)	249.65 (256.273)	-4.907
Hexagonal	8.482 (8.6603)	8.552 (8.6603)	7.779 (7.9022)	89.49 (90)	90.54 (90)	120.06 (120)	244.16 (252.633)	-4.999
MAPbI₃								
Cubic	6.334 (6.3115)	6.342 (6.3115)	6.347 (6.3115)	89.71 (90)	90.06 (90)	89.91 (90)	254.90 (251.60)	-4.942
Tetragonal	8.711 (8.8492)	8.718 (8.8492)	12.401 (12.6420)	90.11 (90)	89.97 (90)	90.03 (90)	235.42 (247.51)	-5.012
Trigonal	8.958	8.958	10.610	90.61	89.44	120.77	243.84	-4.928
Hexagonal	8.375	8.357	7.917	88.94	89.99	120.21	239.39	-4.914

^aAvailable experimental values in parentheses, and are obtained from ref 21. The ground states having the lowest ΔH_f are shown in bold.

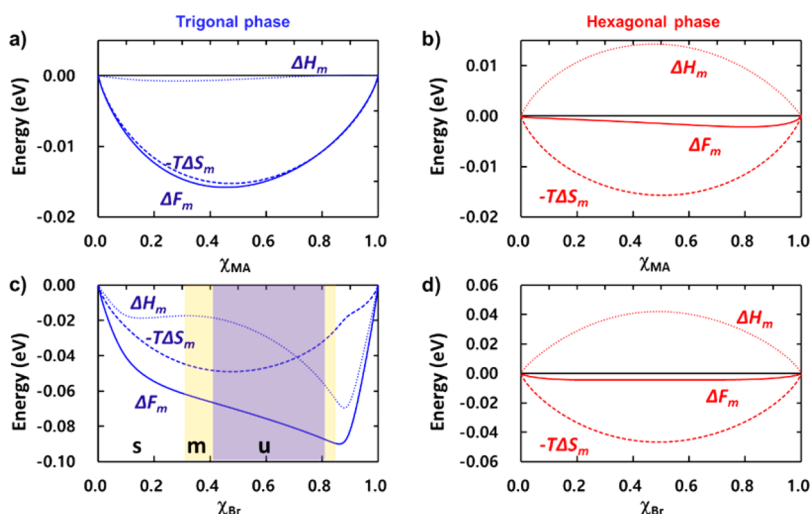


Figure 2. Enthalpy (dotted line), entropy (dashed line), and free energy (solid line) of mixing calculated using GQCA. MA substitution into (a) trigonal and (b) hexagonal phases of FAPbI₃. Br substitution into (c) trigonal and (d) hexagonal phases of FAPbI₃. For the case of Br substitution into trigonal phases, “m” and “u” denote metastable and unstable regimes due to binodal and spinodal decomposition ranges, respectively. “s” denotes the stable regime. DFT energies for 153 different compositions and configurations were used for the configurational ensemble average.

concept become valid only when statistical–mechanical treatments are appropriately considered, in addition to the investigation of only a few configurations using DFT energetics. A useful theoretical framework to calculate the phase stability and the phase mixing behavior of PSCs for the mixed halides was suggested by the Walsh group.⁴³ It is noted that we employed a similar approach in this study, which will be discussed hereafter.

For the trigonal phase, with three different A-sites in the unit cell, we sampled all the possible 8 ($=2^3$) cation configurations. For the hexagonal phase, we considered a ($2 \times 1 \times 1$) supercell to enumerate the configurations because the unit cell has only two different A-sites. This leads to two replicas of two A-sites, yielding 10 irreducible cation configurations considering the symmetry of the supercell expansion (see Figure S1). Since the number of possible halide configurations in the unit cell of trigonal and hexagonal phases is enormously large (512 ($=2^9$) and 64 ($=2^6$), respectively), we reduce the number of configurations by adapting the symmetry of the inorganic framework using the site-occupancy disorder (SOD) method.⁴⁴ This yields 120 and 13 symmetrically different halide configurations for the trigonal and hexagonal phases, respectively, all of which were sampled to investigate halide mixing.

We then obtained DFT optimized structures and energies of the sampled structures with different cation and halide

configurations (153 DFT calculations = 8 + 12 + 120 + 13), which were employed for the statistical free energy calculation using the generalized quasi-chemical approximation (GQCA).⁴⁵ Using the GQCA, which (arbitrarily) divides the crystal into an ensemble of independent clusters, one can formulate the statistical problem of averaging each class of clusters into a polynomial equation. Therefore, GQCA allows the efficient calculation of the enthalpy, entropy, and free energy of mixing of binary alloys with an arbitrary lattice. In previous work, GQCA has been successfully utilized for the thermodynamic analysis of semiconductor alloys,^{46,47} and also for the investigation of halide mixing in the MAPbI₃ system.⁴³

3. RESULTS AND DISCUSSION

3.1. Polymorphic growth of the α - and δ -phases of FAPbI₃. For a given chemical potential of B and X, i.e., μ_B and μ_X , the thermodynamic equilibrium growth condition of each hybrid perovskite (ABX₃) is determined using the inequalities below, which define the ranges of μ_B and μ_X , where a spontaneous dissociation of ABX₃ to AX + BX₂ is avoided:⁴⁸

$$\mu_B + 2\mu_X > \Delta H_f^{ABX_3} - \Delta H_f^{AX} \quad (1)$$

$$\mu_B + 2\mu_X < \Delta H_f^{BX_2} \quad (2)$$

Here ΔH_f is the formation enthalpy and $A \in \{\text{FA}, \text{MA}\}$, $B = \text{Pb}$, and $X \in \{\text{I}, \text{Br}\}$. To determine ΔH_f , we performed further DFT calculations on reference states: PbI_2 , PbBr_2 , MAI , MABr , FAI , FABr , FA , MA , I_2 , and Br_2 (DFT optimized structures and energies are given in Figure S2 and Table S1, respectively).

As shown in Figure 1c, our DFT results clearly show that both α -FAPbI₃ (hexagonal phase) and δ -FAPbI₃ (trigonal phase) can be formed under a compatible range of chemical potentials, which is consistent with experimental results.²² It should be further noted that δ -FAPbI₃ is thermodynamically more stable than α -FAPbI₃ (by 90 meV/f.u.), explaining the spontaneous α - to δ -phase transformation in the long term. Further, the calculated equilibrium growth condition of α -MAPbI₃ (tetragonal phase), as shown in Figure S3, is consistent with experimental data.²² We also note that the calculated cell volumes reasonably agree with the experimental values (within 5%). Despite some possible error sources, such as the intrinsic error of the DFT total energies and the different orientations of organic cations, a good agreement of our DFT results with experimental results of structures and energies indicates the suitability of our choice of DFT method and simulation models in predicting reliable thermodynamic results that will be discussed hereafter.

3.2. Enthalpy, entropy, and free energy of mixing at A- and X-sites. As the small relative formation enthalpy is the origin of polymorphic growth of FAPbI₃, it is of consequent interest to understand how the cation or halide mixing alters the relative thermodynamics of the polymorphic trigonal and hexagonal phases. We thus calculated enthalpy ($\Delta H_{m@A(X)}$), entropy ($\Delta S_{m@A(X)}$), and free energy ($\Delta F_{m@A(X)}$) of mixing at the A(X)-site using the generalized quasi-chemical approximation (GQCA).⁴⁵ Figures 2a and 2b show MA mixing behavior of the α - and δ -FAPbI₃, respectively, at 300 K (where χ_{MA} means the mole fraction of MA; data for other temperature conditions are presented in Figure S4). We find that the mixing enthalpy of MA into the δ -FAPbI₃ is unfavorable, which is marginally compensated by the entropic stabilization. Moreover, we find that alloying of MA into the α -FAPbI₃ is both enthalpically and entropically favored. Such a difference can be ascribed to the more rigid inorganic framework of the face-sharing structure compared with the corner-sharing structure. We also note that the cation mixing is mostly driven by entropy (the absolute magnitude of $\Delta H_{m@A}$ is marginal, as it is less than 15 meV/f.u.). This is in the same line with the previous report by Yi et al. on the entropic contribution to the stabilization.²⁷

Figures 2c and 2d show the halide mixing behavior of the α - and δ -FAPbI₃, respectively, which also predicts that the α -phase more energetically favors the formation of a solid solution phase than the δ -phase does (where χ_{Br} means the mole fraction of Br; data for other temperature conditions are presented in Figure S5). The halide mixing of δ -FAPbI₃ shows a behavior similar to that of the MA mixing, which is enthalpically unfavorable and can be marginally compensated for by the entropic effect. However, for the halide mixing of α -FAPbI₃, interestingly, we find that there exists a miscibility gap that is mostly driven by enthalpy, as identified with a binodal region of $0.31 < \chi_{\text{Br}} < 0.84$ and a spinodal region of $0.41 < \chi_{\text{Br}} < 0.81$. It is noted that a similar tendency has been theoretically suggested for the Br/I mixing in MAPbI₃ by the Walsh group.⁴³ Furthermore, our results explain the previous experimental results, showing that good crystalline mixed halide FA-based PSCs can be obtained only at the I- and Br-rich condition of $\chi_{\text{Br}} < 0.15$ – 0.2 or $\chi_{\text{Br}} > 0.55$ – 0.7 .^{29,32}

3.3. Relative phase stability during single-site alloying.

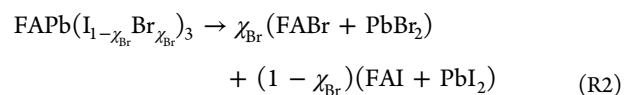
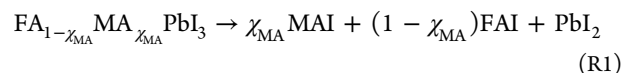
Although the free energy of mixing (ΔF_m) provides a thermodynamic measure of the stability of the solid-solution phase with respect to the mechanical mixture, it provides no direct information about the relative thermodynamic stability between two polymorphic phases. By rearranging the equation defining ΔF_m , we thus formulated the formation free energy (ΔF_f) of mixed perovskites as follows:

$$\Delta F_f^{\text{FA}_{1-\chi_{\text{MA}}}\text{MA}_{\chi_{\text{MA}}}\text{PbI}_3} = \chi_{\text{MA}} \Delta H_f^{\text{MAPbI}_3} + (1 - \chi_{\text{MA}}) \Delta H_f^{\text{FAPbI}_3} + \Delta F_{m@A} \quad (3)$$

$$\Delta F_f^{\text{FAPb}(\text{I}_{1-\chi_{\text{Br}}}\text{Br}_{\chi_{\text{Br}}})_3} = \chi_{\text{Br}} \Delta H_f^{\text{FAPbBr}_3} + (1 - \chi_{\text{Br}}) \Delta H_f^{\text{FAPbI}_3} + \Delta F_{m@X} \quad (4)$$

Since there is no configurational entropy for pure phases, we assumed that $\Delta F_f^{\text{FAPbI}_3} \approx \Delta H_f^{\text{FAPbI}_3}$, $\Delta F_f^{\text{MAPbI}_3} \approx \Delta H_f^{\text{MAPbI}_3}$, and $\Delta F_f^{\text{FAPbBr}_3} \approx \Delta H_f^{\text{FAPbBr}_3}$, all of which were calculated using DFT (Table 1).

To provide a thermodynamic measure with respect to the chemical decomposition of the alloy systems, we considered the decomposition reaction of mixed perovskites as follows:



We then investigated the stability of mixed perovskites to resist chemical decomposition, by comparing the formation free energy (ΔF_f) with the reaction enthalpies of the above dissociation reactions, $\Delta H_d^{(\text{R1})}$ and $\Delta H_d^{(\text{R2})}$.

Figures 3a and 3b compare ΔF_f of trigonal and hexagonal phases and ΔH_d of alloy systems as a function of χ_{MA} or χ_{Br} for cation and halide mixing cases, respectively. During cation mixing (Figure 3a), where the solid solution phase is stabilized by a high configuration entropy (*vide supra*), the lowest energy path follows the phase transition from the hexagonal phase to the trigonal phase (at $\chi_{\text{MA}} = 0.77$), and then to the dissociated phase (at $\chi_{\text{MA}} = 0.90$). This suggests that the MA mixing is effective in stabilizing the trigonal phase over the hexagonal phase; however, it simultaneously hampers the intrinsic thermodynamic stability to resist chemical decomposition. Due to the relatively late transition point from hexagonal to trigonal phase, which is close to the point of dissociation, the composition range where the trigonal phase becomes the most stable phase is highly limited.

For the halide mixing shown in Figure 3b, the lowest energy path follows the phase transition from the hexagonal phase to the trigonal phase (at $\chi_{\text{Br}} = 0.51$), and then back to the hexagonal phase (at $\chi_{\text{Br}} = 0.95$). We note that the stability to resist chemical decomposition is substantial enough since ΔH_d is always higher than ΔF_f even though the gap is decreasing as χ_{Br} increases. However, we recall that there exists a miscibility gap for the range of $0.31 < \chi_{\text{Br}} < 0.84$ at 300 K during halide mixing, which prohibits the bromide mixing with a concentration high enough to induce a phase transformation. Additionally, we discuss that a high concentration of Br accompanies a substantial band gap widening,^{1,2,16} significantly degrading the photovoltaic efficiency. Therefore, it is suggested that we need a more effective way to stabilize the trigonal phase while keeping the bromide

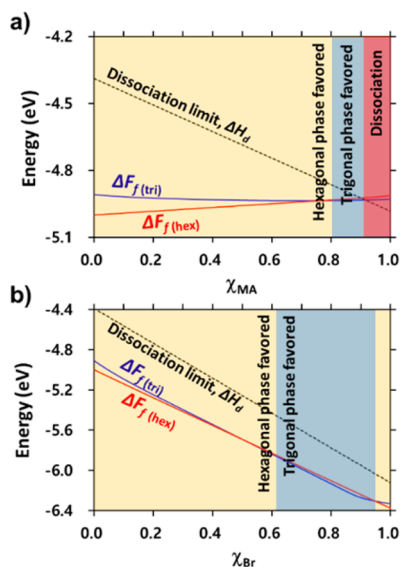


Figure 3. Formation free energies (ΔF_f) of trigonal phase (blue) and hexagonal phase (red), and the reaction enthalpy for the chemical decompositions (ΔH_d , black). (a) MA substitution leads to the phase transition from hexagonal to trigonal at $\chi_{MA} = 0.77$, which then decomposes the perovskite structure at $\chi_{MA} = 0.90$. (b) Br substitution stabilizes the trigonal phase for the region of $0.51 < \chi_{Br} < 0.95$. However, due to the existence of the miscibility gap at $0.31 < \chi_{Br} < 0.84$, high enough concentration of Br cannot be achieved.

concentration low, in order to successfully avoid the composition range corresponding to the miscibility gap and to prohibit widening of the electronic band gap.

3.4. Phase stability map during dual-site alloying. We now expand our discussion to the effect of dual-site alloying of cations and halides. To formulate the formation free energy of $FA_{1-\chi_{MA}}MA_{\chi_{MA}}Pb(I_{1-\chi_{Br}}Br_{\chi_{Br}})_3$, we generalized eqs 3 and 4 into eq 5 using the two-site solid-solution (or reciprocal solution) model:⁴⁹

$$\begin{aligned} \Delta F_f^{FA_{1-\chi_{MA}}MA_{\chi_{MA}}Pb(I_{1-\chi_{Br}}Br_{\chi_{Br}})_3} &= \chi_{MA}\chi_{Br}\Delta H_f^{MAPbBr_3} + (1-\chi_{MA})\chi_{Br}\Delta H_f^{FAPbBr_3} \\ &+ (1-\chi_{MA})(1-\chi_{Br})\Delta H_f^{FAPbI_3} \\ &+ \chi_{MA}(1-\chi_{Br})\Delta H_f^{MAPbI_3} + \Delta F_{m@A,X} \end{aligned} \quad (5)$$

where $\Delta F_{m@A,X}$ denotes the dual-site mixing free energy. Multivariate Taylor expansion of $\Delta F_{m@A,X}$ near $\chi_{MA} = \chi_{Br} = 0$ leads to

$$\begin{aligned} \Delta F_{m@A,X} &= \sum_n \frac{\chi_{MA}^n}{n!} \frac{\partial^n \Delta F_{m@A,X}}{(\partial \chi_{MA})^n} \Big|_{0,0} \\ &+ \sum_k \frac{\chi_{MA}^k}{k!} \frac{\partial^k \Delta F_{m@A,X}}{(\partial \chi_{Br})^k} \Big|_{0,0} + O(\chi_{MA}^m \chi_{Br}^l) \\ &= \Delta F_{m@A}^I|_{\chi_{Br}=0} + \Delta F_{m@X}^I|_{\chi_{MA}=0} + O(\chi_{MA}^m \chi_{Br}^l) \end{aligned} \quad (6)$$

for $m = 1, 2, 3, \dots$ and $l = 1, 2, 3, \dots$. Here the last term denotes the contributions of the coupling terms between χ_{MA} and χ_{Br} , which can be determined rigorously by obtaining exhaustive sets of energetics for the wide range of χ_{MA} and χ_{Br} . However, it is nearly

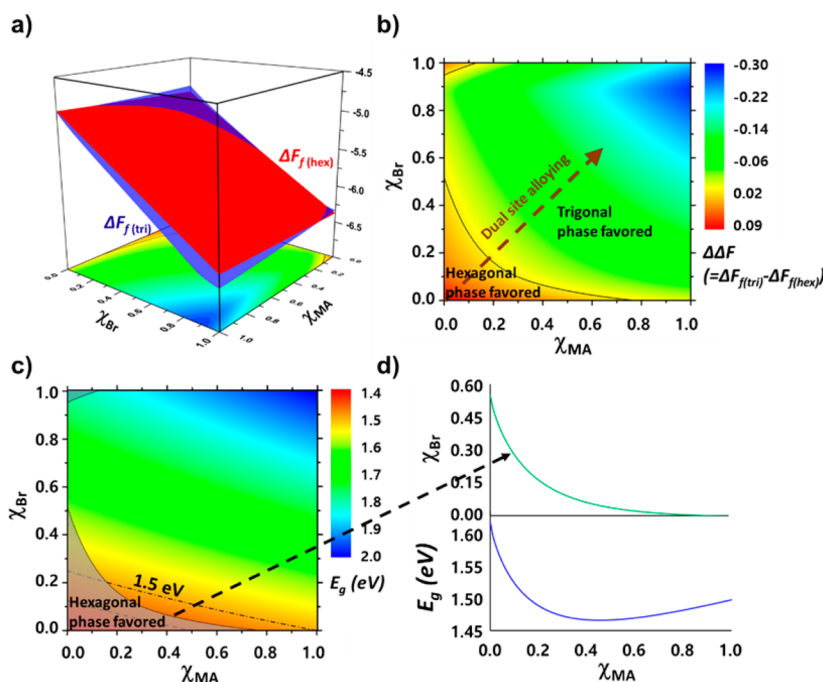


Figure 4. Change in relative phase stability and band gap during dual site alloying (phase map). (a) Formation free energies of trigonal phase (blue; $\Delta F_{f(tri)}$) and hexagonal phase (red; $\Delta F_{f(hex)}$) of $FA_{1-\chi_{MA}}MA_{\chi_{MA}}Pb(I_{1-\chi_{Br}}Br_{\chi_{Br}})_3$. (b) Color map showing the relative free energy between trigonal and hexagonal phases, $\Delta\Delta F (= \Delta F_{f(tri)} - \Delta F_{f(hex)})$. The phase transition line is defined as the line satisfying $\Delta\Delta F = 0$ (black solid line). (c) Cation and halide mixing changes the band gap of trigonal α -phase perovskite. Using the DFT calculated band gaps (E_g) of four different perovskites, E_g of mixed perovskites is estimated using Vegard's law. (d) Change in Br content (χ_{Br} ; green) and estimated band gap (E_g ; blue) as a function of MA content (χ_{MA}) along the phase transition line.

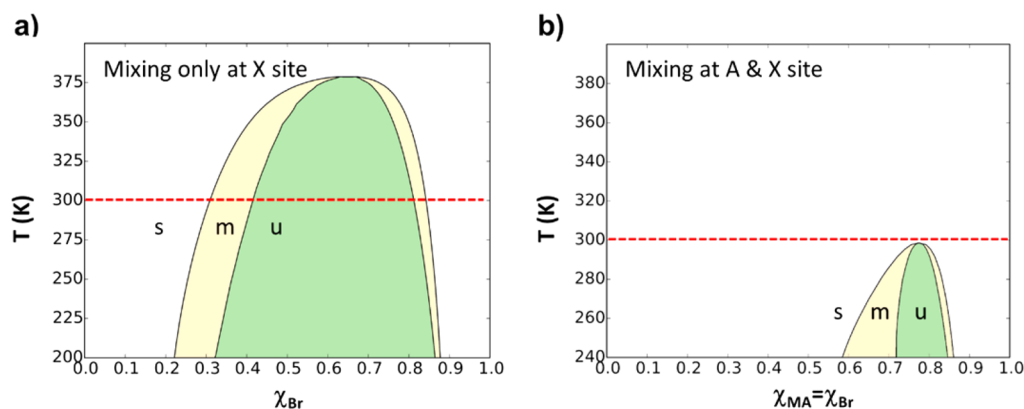


Figure 5. Change in miscibility gap. Phase diagrams of the trigonal FAPbI_3 (a) during mixing only at the X-site, i.e., $\text{FAPb}(\text{I}_{1-\chi_{\text{Br}}}\text{Br}_{\chi_{\text{Br}}})_3$, and (b) during mixing both at A- and X-sites with equal amounts of MA and Br, i.e., $\text{FA}_{1-\chi_{\text{MA}}}\text{MA}_{\chi_{\text{MA}}}\text{Pb}(\text{I}_{1-\chi_{\text{Br}}}\text{Br}_{\chi_{\text{Br}}})_3$. Phase boundaries for the binodal decomposition and spinodal decomposition are displayed; regimes when the solid solution phase is stable (s; white), metastable (m; yellow), and unstable (u; green). Red dashed horizontal line shows the miscibility gap at room temperature.

impractical to sample such a vast range of configurational space using first-principles based calculations. In this study, we therefore assumed that there is no contribution from the coupling term, which is valid for the dilute region at least. By plugging GQCA results for $\Delta F_{m@A}$ and $\Delta F_{m@X}$ into eqs 5 and 6, we calculate the formation free energy of dual-site alloy systems of $\Delta F_f^{\text{FA}_{1-\chi_{\text{MA}}}\text{MA}_{\chi_{\text{MA}}}\text{Pb}(\text{I}_{1-\chi_{\text{Br}}}\text{Br}_{\chi_{\text{Br}}})_3}$ for trigonal and hexagonal phases, i.e., $\Delta F_{f(\text{tri})}$ and $\Delta F_{f(\text{hex})}$, respectively. Then, the relative free energy between two polymorphic phases is defined as $\Delta\Delta F$ ($\equiv \Delta F_{f(\text{tri})} - \Delta F_{f(\text{hex})}$).

Figure 4a shows the change in $\Delta F_{f(\text{tri})}$ and $\Delta F_{f(\text{hex})}$, and Figure 4b shows the color map of $\Delta\Delta F$ as a function of χ_{MA} and χ_{Br} . To illustrate how the compositional engineering alters the material's properties, the band gap change during dual site alloying is also predicted using Vegard's law in Figure 4c. The phase boundary (defined as the line satisfying $\Delta\Delta F = 0$) shows that the compositional engineering at a single site (either A- or X-sites) requires a high MA or Br content degrading the optimal material property of α - FAPbI_3 , while the compositional engineering at dual sites (both A- and X-sites) allows the efficient phase transition even with a low Br content. In contrast to the only halide mixing case (Figure 5a), for the case of alloying with an equal amount of MA and Br, i.e., $\chi_{\text{MA}} = \chi_{\text{Br}}$, we find that the α -phase can be stabilized at $\chi_{\text{MA}} = \chi_{\text{Br}} = \sim 0.2$, and the miscibility gap disappears at room temperature (Figure 5b); the former is in good agreement with the previous experimental results reported by Seok's group, where the XRD measurement confirmed that the formation of the δ -phase can be entirely suppressed at $\chi_{\text{MA}} = \chi_{\text{Br}} = 0.15$ (i.e., $\text{FA}_{0.85}\text{MA}_{0.15}\text{PbI}_{2.55}\text{Br}_{0.45}$),¹¹ and the latter well explains the experimental results about the crystallinity of FA-based PSCs depending on the Br contents reported by the Snaith group.²⁹ Furthermore, among four end members of the two-dimensional phase map, we find that MAPbBr_3 shows the largest energy difference between the δ - and α -phases. Bearing in mind that the mixing enthalpies and entropies between different perovskites are relatively small (under 100 meV), this implies that MAPbBr_3 can be considered as an antistabilizer for δ - FAPbI_3 . This suggests that we would be able to select the preferred crystal structures by adding another possible antistabilizing component, that destabilizes unwanted lattice structures.

Figure 4d shows the change in the Br content (χ_{Br}) and the predicted band gap as a function of MA content (χ_{MA}) at the

phase boundary. This implies that there could be extra room for the compositional engineering of the lower band gap and thereby a higher efficiency. This can be achieved by slightly increasing the MA content while decreasing the Br content; albeit, the quantitative prediction made here contains a certain degree of error propagated from the error in the DFT calculation of the band gap.

3.5. Limitations of the Goldschmidt tolerance factor in organic–inorganic hybrid perovskite systems. The Goldschmidt tolerance factor is a well-known indicator for the stabilization of cubic perovskites,⁵⁰ and there have been several studies to explain the enhanced stability of PSCs using the tolerance factor.^{27,51,52} As such, we attempted to interpret our results using the concept of the tolerance factor. The Goldschmidt tolerance factor, t , for ABX_3 perovskite is defined as $(r_A + r_X) / (\sqrt{2}(r_B + r_X))$, where $r_{A/B/X}$ means the ionic radius of A, B, or X. Using the previously determined ionic radii of MA, FA, Pb, I, and Br ($r_{\text{MA}} = 2.17 \text{ \AA}$, $r_{\text{FA}} = 2.53 \text{ \AA}$, $r_{\text{Pb}^{2+}} = 1.19 \text{ \AA}$, $r_{\text{I}^-} = 2.2 \text{ \AA}$, $r_{\text{Br}^-} = 1.96 \text{ \AA}$),⁵¹ the tolerance factor of FAPbI_3 becomes $t_{\text{FAPbI}_3} = 0.987$, supporting the polymorphic formation of hexagonal and trigonal phases, since the value is close to unity. The effective cation size can be reduced by substituting MA for FA, which decreases the tolerance factor to 0.912. This explains the DFT results showing that the trigonal phase becomes gradually more stabilized over the hexagonal phase as the MA concentration increases. Since the tolerance factor of MAPbBr_3 is 0.927, which is smaller than t_{FAPbI_3} , simultaneous mixing of cations and halides is expected to be helpful in suppressing the hexagonal phase.

However, substituting Br for I increases the tolerance factor to 1.008, which indicates the more favorable formation of the hexagonal phase. This is in contrast to our DFT results and the previous experimental results. We conceive that the failure of the simple Goldschmidt tolerance factor is due to the strong nonideal behavior of halide mixing (strong enthalpic effect as aforementioned). This presumably originated from the substantial covalent character of the Pb–X bond, which is in contrast to the cation mixing case.⁵³ This suggests the need for the extended concept of the tolerance factor in explaining the halide mixing, in order to make it a predictive tool in designing stable PSC materials, which requires further in-depth research.

4. CONCLUSION

In summary, we elucidated the effect of cation/anion mixing on phase stability using first-principles-based DFT energetics combined with the statistical ensemble average method of GQCA. We found that the cation mixing at the A-site is mostly driven by configurational entropy because the mixing enthalpy is not substantial. We also found that the halide mixing at the X-site of α -FAPbI₃ is mostly driven by enthalpy, yielding a substantial miscibility gap. To avoid the immiscibility, and also to maintain the good band gap property of α -FAPbI₃, it becomes critically important to induce a δ - to α -phase transition while keeping the Br content low. We found that dual-site alloying of MA and Br both at A- and X-sites cooperatively stabilizes the α -phase, thereby allowing the δ - to α -phase transition with a low Br content. For further optimization of the PSCs, it is suggested that lowering the Br content, and thereby further decreasing the band gap, is required. We anticipate that our study provides fundamental guidelines for compositional engineering toward the development of PSCs with an improved performance. For instance, we conceive that mixing many different elements at the A-site would be helpful in stabilizing the materials by maximizing the configurational entropy, similar to the concept of high-entropy alloys.⁵⁴ We further envision that computational screening the component that can highly destabilize the unwanted phase, i.e., antistabilizer, would be the next direction to specifically stabilize the promising but unstable perovskite systems, which can be applied to design new types of perovskite solar cell materials, e.g., Pb-free PSCs. We believe that the proposed principles will be useful in controlling and optimizing activity and stability, which will eventually contribute to the successful commercialization of PSCs.

■ ASSOCIATED CONTENT

Supporting Information

The Supporting Information is available free of charge on the ACS Publications website at DOI: 10.1021/acs.jpcc.7b03176.

Supplementary figures of DFT optimized structures; phase diagram showing single-phase growth of MAPbI₃; temperature dependent mixing thermodynamics; and sampled cation configurations of trigonal phase; and supplementary table listing DFT results on reference and secondary phases (PDF)

■ AUTHOR INFORMATION

Corresponding Authors

*(K.-H.H.) E-mail: kiha.hong@hanbat.ac.kr. Telephone: +82-42-821-1238.

*(H.K.) E-mail: linus16@kaist.ac.kr. Telephone: +82-42-350-1725.

ORCID

Hyungjun Kim: 0000-0001-8261-9381

Notes

The authors declare no competing financial interest.

■ ACKNOWLEDGMENTS

This work was supported by the HMC (Hyundai Motor Company). J. Jeon, T. Eom, and H. Kim acknowledge the support by the Nanomaterial Technology Development Program (Grant 2016M3A7B4025414), and K.-H. Hong acknowledges the support by the Basic Science Research Program (NRF-2015R1A1A1A05001241) through the National

Research Foundation of Korea (NRF) funded by the Ministry of Science, ICT & Future Planning.

■ REFERENCES

- (1) Kojima, A.; Teshima, K.; Shirai, Y.; Miyasaka, T. Organometal Halide Perovskites as Visible-Light Sensitizers for Photovoltaic Cells. *J. Am. Chem. Soc.* **2009**, *131*, 6050–6051.
- (2) Kim, H. S.; Lee, C. R.; Im, J. H.; Lee, K. B.; Moehl, T.; Marchioro, A.; Moon, S. J.; Humphry-Baker, R.; Yum, J. H.; Moser, J. E.; et al. Lead Iodide Perovskite Sensitized All-Solid-State Submicron Thin Film Mesoscopic Solar Cell with Efficiency Exceeding 9%. *Sci. Rep.* **2012**, *2*, 591.
- (3) Domanski, K.; Tress, W.; Moehl, T.; Saliba, M.; Nazeeruddin, M. K.; Grätzel, M. Working Principles of Perovskite Photodetectors: Analyzing the Interplay between Photoconductivity and Voltage-Driven Energy-Level Alignment. *Adv. Funct. Mater.* **2015**, *25*, 6936–6947.
- (4) Kim, H. S.; Mora-Sero, I.; Gonzalez-Pedro, V.; Fabregat-Santiago, F.; Juarez-Perez, E. J.; Park, N. G.; Bisquert, J. Mechanism of Carrier Accumulation in Perovskite Thin-Absorber Solar Cells. *Nat. Commun.* **2013**, *4*, 2242.
- (5) Burschka, J.; Pellet, N.; Moon, S. J.; Humphry-Baker, R.; Gao, P.; Nazeeruddin, M. K.; Grätzel, M. Sequential Deposition as a Route to High-Performance Perovskite-Sensitized Solar Cells. *Nature* **2013**, *499*, 316–319.
- (6) Shi, D.; Adinolfi, V.; Comin, R.; Yuan, M.; Alarousu, E.; Buin, A.; Chen, Y.; Hoogland, S.; Rothenberger, A.; Katsiev, K.; et al. Low Trap-State Density and Long Carrier Diffusion in Organolead Trihalide Perovskite Single Crystals. *Science* **2015**, *347*, 519–522.
- (7) Bailie, C. D.; Christoforo, M. G.; Mailoa, J. P.; Bowring, A. R.; Unger, E. L.; Nguyen, W. H.; Burschka, J.; Pellet, N.; Lee, J. Z.; Grätzel, M.; et al. Semi-Transparent Perovskite Solar Cells for Tandems with Silicon and Cigs. *Energy Environ. Sci.* **2015**, *8*, 956–963.
- (8) Mei, A.; Li, X.; Liu, L.; Ku, Z.; Liu, T.; Rong, Y.; Xu, M.; Hu, M.; Chen, J.; Yang, Y.; et al. A Hole-Conductor-Free, Fully Printable Mesoscopic Perovskite Solar Cell with High Stability. *Science* **2014**, *345*, 295–298.
- (9) Im, J. H.; Lee, C. R.; Lee, J. W.; Park, S. W.; Park, N. G. 6.5% Efficient Perovskite Quantum-Dot-Sensitized Solar Cell. *Nanoscale* **2011**, *3*, 4088–4093.
- (10) Jeon, N. J.; Noh, J. H.; Kim, Y. C.; Yang, W. S.; Ryu, S.; Seok, S. I. Solvent Engineering for High-Performance Inorganic-Organic Hybrid Perovskite Solar Cells. *Nat. Mater.* **2014**, *13*, 897–903.
- (11) Jeon, N. J.; Noh, J. H.; Yang, W. S.; Kim, Y. C.; Ryu, S.; Seo, J.; Seok, S. I. Compositional Engineering of Perovskite Materials for High-Performance Solar Cells. *Nature* **2015**, *517*, 476–480.
- (12) Lee, M. M.; Teuscher, J.; Miyasaka, T.; Murakami, T. N.; Snaith, H. J. Efficient Hybrid Solar Cells Based on Meso-Superstructured Organometal Halide Perovskites. *Science* **2012**, *338*, 643–647.
- (13) Liu, M.; Johnston, M. B.; Snaith, H. J. Efficient Planar Heterojunction Perovskite Solar Cells by Vapour Deposition. *Nature* **2013**, *501*, 395–398.
- (14) Yang, W. S.; Noh, J. H.; Jeon, N. J.; Kim, Y. C.; Ryu, S.; Seo, J.; Seok, S. I. High-Performance Photovoltaic Perovskite Layers Fabricated through Intramolecular Exchange. *Science* **2015**, *348*, 1234–1237.
- (15) Zhou, H.; Chen, Q.; Li, G.; Luo, S.; Song, T. B.; Duan, H. S.; Hong, Z.; You, J.; Liu, Y.; Yang, Y. Interface Engineering of Highly Efficient Perovskite Solar Cells. *Science* **2014**, *345*, 542–546.
- (16) Kitazawa, N.; Watanabe, Y.; Nakamura, Y. Optical Properties of Ch₃nh₃pbx₃ (X = Halogen) and Their Mixed-Halide Crystals. *J. Mater. Sci.* **2002**, *37*, 3585–3587.
- (17) Noh, J. H.; Im, S. H.; Heo, J. H.; Mandal, T. N.; Seok, S. I. Chemical Management for Colorful, Efficient, and Stable Inorganic-Organic Hybrid Nanostructured Solar Cells. *Nano Lett.* **2013**, *13*, 1764–1769.
- (18) Pellet, N.; Teuscher, J.; Maier, J.; Grätzel, M. Transforming Hybrid Organic Inorganic Perovskites by Rapid Halide Exchange. *Chem. Mater.* **2015**, *27*, 2181–2188.
- (19) Tanaka, K.; Takahashi, T.; Ban, T.; Kondo, T.; Uchida, K.; Miura, N. Comparative Study on the Excitons in Lead-Halide-Based Perov-

skite-Type Crystals $\text{CH}_3\text{NH}_3\text{PbBr}_3$, $\text{CH}_3\text{NH}_3\text{PbI}_3$. *Solid State Commun.* **2003**, *127*, 619–623.

(20) Buin, A.; Comin, R.; Xu, J. X.; Ip, A. H.; Sargent, E. H. Halide-Dependent Electronic Structure of Organolead Perovskite Materials. *Chem. Mater.* **2015**, *27*, 4405–4412.

(21) Eperon, G. E.; Stranks, S. D.; Menelaou, C.; Johnston, M. B.; Herz, L. M.; Snaith, H. J. Formamidinium Lead Trihalide: A Broadly Tunable Perovskite for Efficient Planar Heterojunction Solar Cells. *Energy Environ. Sci.* **2014**, *7*, 982–988.

(22) Stoumpos, C. C.; Malliakas, C. D.; Kanatzidis, M. G. Semiconducting Tin and Lead Iodide Perovskites with Organic Cations: Phase Transitions, High Mobilities, and near-Infrared Photoluminescent Properties. *Inorg. Chem.* **2013**, *52*, 9019–9038.

(23) Lee, J. W.; Seol, D. J.; Cho, A. N.; Park, N. G. High-Efficiency Perovskite Solar Cells Based on the Black Polymorph of $\text{HC}(\text{NH}_2)_2\text{PbI}_3$. *Adv. Mater.* **2014**, *26*, 4991–4998.

(24) Koh, T. M.; Fu, K.; Fang, Y.; Chen, S.; Sum, T. C.; Mathews, N.; Mhaisalkar, S. G.; Boix, P. P.; Baikie, T. Formamidinium-Containing Metal-Halide: An Alternative Material for near-IR Absorption Perovskite Solar Cells. *J. Phys. Chem. C* **2014**, *118*, 16458–16462.

(25) Binek, A.; Hanusch, F. C.; Docampo, P.; Bein, T. Stabilization of the Trigonal High-Temperature Phase of Formamidinium Lead Iodide. *J. Phys. Chem. Lett.* **2015**, *6*, 1249–1253.

(26) Li, Z.; Yang, M.; Park, J. S.; Wei, S. H.; Berry, J. J.; Zhu, K. Stabilizing Perovskite Structures by Tuning Tolerance Factor: Formation of Formamidinium and Cesium Lead Iodide Solid-State Alloys. *Chem. Mater.* **2016**, *28*, 284–292.

(27) Yi, C.; Luo, J.; Meloni, S.; Boziki, A.; Ashari-Astani, N.; Grätzel, C.; Zakeeruddin, S. M.; Rothlisberger, U.; Grätzel, M. Entropic Stabilization of Mixed A-Cation ABX_3 Metal Halide Perovskites for High Performance Perovskite Solar Cells. *Energy Environ. Sci.* **2016**, *9*, 656–662.

(28) Bi, D.; Tress, W.; Dar, M. I.; Gao, P.; Luo, J.; Renevier, C.; Schenk, K.; Abate, A.; Giordano, F.; Baena, J. P. C.; et al. Efficient Luminescent Solar Cells Based on Tailored Mixed-Cation Perovskites. *Sci. Adv.* **2016**, *2*, e1501170.

(29) McMeekin, D. P.; Sadoughi, G.; Rehman, W.; Eperon, G. E.; Saliba, M.; Hörlantner, M. T.; Haghighirad, A.; Sakai, N.; Korte, L.; Rech, B.; et al. A Mixed-Cation Lead Mixed-Halide Perovskite Absorber for Tandem Solar Cells. *Science* **2016**, *351*, 151–155.

(30) Saliba, M.; Matsui, T.; Seo, J. Y.; Domanski, K.; Correa-Baena, J. P.; Nazeeruddin, M. K.; Zakeeruddin, S. M.; Tress, W.; Abate, A.; Hagfeldt, A.; et al. Cesium-Containing Triple Cation Perovskite Solar Cells: Improved Stability, Reproducibility and High Efficiency. *Energy Environ. Sci.* **2016**, *9*, 1989–1997.

(31) Yang, Z.; Chueh, C. C.; Liang, P. W.; Crump, M.; Lin, F.; Zhu, Z.; Jen, A. K. Y. Effects of Formamidinium and Bromide Ion Substitution in Methylammonium Lead Triiodide toward High-Performance Perovskite Solar Cells. *Nano Energy* **2016**, *22*, 328–337.

(32) Rehman, W.; Milot, R. L.; Eperon, G. E.; Wehrenfennig, C.; Boland, J. L.; Snaith, H. J.; Johnston, M. B.; Herz, L. M. Charge-Carrier Dynamics and Mobilities in Formamidinium Lead Mixed-Halide Perovskites. *Adv. Mater.* **2015**, *27*, 7938–7944.

(33) Frost, J. M.; Butler, K. T.; Brivio, F.; Hendon, C. H.; van Schilfgaarde, M.; Walsh, A. Atomistic Origins of High-Performance in Hybrid Halide Perovskite Solar Cells. *Nano Lett.* **2014**, *14*, 2584–2590.

(34) Haruyama, J.; Sodeyama, K.; Han, L. Y.; Tateyama, Y. First-Principles Study of Ion Diffusion in Perovskite Solar Cell Sensitizers. *J. Am. Chem. Soc.* **2015**, *137*, 10048–10051.

(35) Yin, W. J.; Yang, J. H.; Kang, J.; Yan, Y. F.; Wei, S. H. Halide Perovskite Materials for Solar Cells: A Theoretical Review. *J. Mater. Chem. A* **2015**, *3*, 8926–8942.

(36) Jeon, J.; Goddard, W. A.; Kim, H. Inner-Sphere Electron-Transfer Single Iodide Mechanism for Dye Regeneration in Dye-Sensitized Solar Cells. *J. Am. Chem. Soc.* **2013**, *135*, 2431–2434.

(37) De Angelis, F. Modeling Materials and Processes in Hybrid/Organic Photovoltaics: From Dye-Sensitized to Perovskite Solar Cells. *Acc. Chem. Res.* **2014**, *47*, 3349–3360.

(38) Giorgi, G.; Yamashita, K. Organic-Inorganic Halide Perovskites: An Ambipolar Class of Materials with Enhanced Photovoltaic Performances. *J. Mater. Chem. A* **2015**, *3*, 8981–8991.

(39) Jeon, J.; Park, Y. C.; Han, S. S.; Goddard, W. A.; Lee, Y. S.; Kim, H. Rapid Dye Regeneration Mechanism of Dye-Sensitized Solar Cells. *J. Phys. Chem. Lett.* **2014**, *5*, 4285–4290.

(40) Zheng, F.; Tan, L. Z.; Liu, S.; Rappe, A. M. Rashba Spin-Orbit Coupling Enhanced Carrier Lifetime in $\text{CH}_3\text{NH}_3\text{PbI}_3$. *Nano Lett.* **2015**, *15*, 7794–7800.

(41) Kim, J.; Lee, S. H.; Lee, J. H.; Hong, K. H. The Role of Intrinsic Defects in Methylammonium Lead Iodide Perovskite. *J. Phys. Chem. Lett.* **2014**, *5*, 1312–1317.

(42) Perdew, J. P.; Ruzsinszky, A.; Csonka, G. I.; Vydrov, O. A.; Scuseria, G. E.; Constantin, L. A.; Zhou, X. L.; Burke, K. Restoring the Density-Gradient Expansion for Exchange in Solids and Surfaces. *Phys. Rev. Lett.* **2008**, *100*, 136406.

(43) Brivio, F.; Caetano, C.; Walsh, A. Thermodynamic Origin of Photoinstability in the $\text{CH}_3\text{NH}_3\text{Pb}(\text{I}_{1-x}\text{Br}_x)_3$ Hybrid Halide Perovskite Alloy. *J. Phys. Chem. Lett.* **2016**, *7*, 1083–1087.

(44) Grau-Crespo, R.; Hamad, S.; Catlow, C. R. A.; de Leeuw, N. H. Symmetry-Adapted Configurational Modelling of Fractional Site Occupancy in Solids. *J. Phys.: Condens. Matter* **2007**, *19*, 256201.

(45) Sher, A.; Vanschilfgaarde, M.; Chen, A. B.; Chen, W. Quasi-Chemical Approximation in Binary-Alloys. *Phys. Rev. B: Condens. Matter Mater. Phys.* **1987**, *36*, 4279–4295.

(46) Schleife, A.; Eisenacher, M.; Rodl, C.; Fuchs, F.; Furthmüller, J.; Bechstedt, F. Ab Initio Description of Heterostructural Alloys: Thermodynamic and Structural Properties of $\text{Mg}_{x\text{Zn}1-x}\text{O}$ and $\text{Cd}_{x\text{Zn}1-x}\text{O}$. *Phys. Rev. B: Condens. Matter Mater. Phys.* **2010**, *81*, 15.

(47) Teles, L. K.; Furthmüller, J.; Scolfaro, L. M. R.; Leite, J. R.; Bechstedt, F. First-Principles Calculations of the Thermodynamic and Structural Properties of Strained $\text{In}_{1-x}\text{Ga}_x\text{N}$ and $\text{Al}_x\text{Ga}_{1-x}\text{N}$ Alloys. *Phys. Rev. B: Condens. Matter Mater. Phys.* **2000**, *62*, 2475–2485.

(48) Yin, W. J.; Shi, T.; Yan, Y. Unusual Defect Physics in $\text{CH}_3\text{NH}_3\text{PbI}_3$ Perovskite Solar Cell Absorber. *Appl. Phys. Lett.* **2014**, *104*, 063903.

(49) Wood, B. J.; Nicholls, J. Thermodynamic Properties of Reciprocal Solid-Solutions. *Contrib. Mineral. Petrol.* **1978**, *66*, 389–400.

(50) Goldschmidt, V. M. Die Gesetze Der Kristallochemie. *Naturwissenschaften* **1926**, *14*, 477–485.

(51) Nagabushana, G. P.; Shivaramaiah, R.; Navrotsky, A. Direct Calorimetric Verification of Thermodynamic Instability of Lead Halide Hybrid Perovskites. *Proc. Natl. Acad. Sci. U. S. A.* **2016**, *113*, 7717–7721.

(52) Travis, W.; Glover, E. N. K.; Bronstein, H.; Scanlon, D. O.; Palgrave, R. G. On the Application of the Tolerance Factor to Inorganic and Hybrid Halide Perovskites: A Revised System. *Chem. Sci.* **2016**, *7*, 4548–4556.

(53) Kieslich, G.; Sun, S.; Cheetham, A. K. An Extended Tolerance Factor Approach for Organic-Inorganic Perovskites. *Chem. Sci.* **2015**, *6*, 3430–3433.

(54) Zhang, Y.; Zhou, Y. J.; Lin, J. P.; Chen, G. L.; Liaw, P. K. Solid-Solution Phase Formation Rules for Multi-Component Alloys. *Adv. Eng. Mater.* **2008**, *10*, 534–538.